Chemical Engineering Journal 525 (2025) 170646

Contents lists available at ScienceDirect

Chemical Engineering Journal

journal homepage: www.elsevier.com/locate/cej

pH-responsive compartmentalized alginate beads enable spatial control of sequential nanozyme reactions

Hui Yang [a,b], Catherine P. Whitby [b,c], Jadranka Travas-Sejdic [a,b,*]

[a] Centre for Innovative Materials for Health, School of Chemical Sciences, The University of Auckland, 23 Symonds Street, Auckland, New Zealand
[b] MacDiarmid Institute for Advanced Materials and Nanotechnology, Victoria University of Wellington, PO Box 600, Wellington, New Zealand
[c] School of Food Technology and Natural Sciences, Massey University, Palmerston North, New Zealand

ARTICLE INFO

Keywords:
Compartmentalized nanozymes
Sequential catalysis
Hydrogel beads
pH-responsive
Coaxial electrospray

ABSTRACT

Controlling two-step sequential catalytic reactions through external stimuli is a powerful approach for developing responsive chemical systems with potential applications in, for example, logic-gated sensing, process-sequence checking and programmable pollutant remediation. Here, a pH-responsive compartmentalized hydrogel bead system was fabricated *via* coaxial microfluidic electrospray, in which gold (Au) and iron oxide (Fe_3O_4) nanozymes were spatially segregated into distinct domains. We systematically assessed the pH-dependent reactivity of Au and Fe_3O_4 nanozymes between pH 2 and 9 to evaluate individual catalytic activities. Au nanoparticles (AuNPs) exhibited glucose oxidase (GOx)-like activity at pH 8–9, quantified by a cobalt-carbonate (Co/CO_3) UV–vis assay, while Fe_3O_4 NPs showed strong peroxidase (POD)-like activity at pH 2–3, quantified by 2,2′-azino-bis(3-ethylbenzothiazoline-6-sulfonic acid) diammonium salt (ABTS) oxidation. Leveraging this pH-selective behaviour, the Au-rich domain catalyses glucose oxidation to generate hydrogen peroxide (H_2O_2), which then diffuses into the Fe_3O_4-rich domain for decomposition. Compared to free and single hydrogel system, the compartmentalized system enhances the reaction efficiency by minimizing interference between nanozymes through spatial separation.

1. Introduction

Living cells rely on compartmentalized organelles [1], each enclosed by membranes [2] and performing distinct functions essential for maintaining cellular physiology [3]. Since each organelle encapsulates specific enzymes, they can conduct distinct chemical reactions tailored to the cell's needs [4]. In these processes, the product of the first reaction often serves as the starting material for the next, with sequential reactions occurring in different compartments [5]. Unlike traditional step-by-step synthesis, this approach eliminates the need for intermediate purification and isolation procedures, streamlining the overall process [6]. One interesting but challenging topic is the assembly of different enzymes together into ordered functional systems, a common phenomenon in nature but much more difficult to achieve with artificial components [7–9]. Hydrogels are excellent catalyst hosts due to their facile crosslinking, good mechanical stability and microporous structure [10]. These features make it possible to construct multi-compartmental systems that can hold different catalysts [11–13]. The microporous network also allows small molecules to diffuse efficiently, enabling sequential reactions to occur in a controlled manner [14,15].

While natural enzymes are highly efficient and specific, they often suffer from poor long-term stability, vulnerability to harsh environments, high production costs and storage challenges [16]. In contrast, nanozymes (inorganic nanomaterials that catalyse reactions on their surfaces) [17] have gained attention due to their enhanced stability, robustness under extreme conditions, facile synthesis and functionalization, and overall cost-effectiveness [18–20] Significantly, some nanozymes exhibit stimuli-responsive catalytic activity, meaning their catalytic function can be activated or terminated by external factors such as pH, light, temperature or ultrasound [21]. For example, AuNPs exhibit GOx-like activity under neutral to alkaline environments, catalysing glucose oxidation and reducing O_2 to generate H_2O_2 [22]. Fe_3O_4 NPs mimic POD-like activity under acidic conditions, catalysing substrate oxidation in the presence of H_2O_2 [23]. Similarly, titanium dioxide acts as a photocatalyst under UV light, where UV irradiation excites electrons, generating reactive oxygen species that drive

* Corresponding author at: Centre for Innovative Materials for Health, School of Chemical Sciences, The University of Auckland, 23 Symonds Street, Auckland, New Zealand.
E-mail address: j.travas-sejdic@auckland.ac.nz (J. Travas-Sejdic).

https://doi.org/10.1016/j.cej.2025.170646
Received 22 August 2025; Received in revised form 13 October 2025; Accepted 7 November 2025
Available online 9 November 2025

oxidation reactions [24]. Additionally, thermo-responsive polymers can regulate nanozymes' catalytic activity by blocking active sites below the lower critical solution temperature (LCST) and exposing them when above LCST, enabling temperature-controlled activation [25]. Likewise, organic sonosensitizers initially block nanozymes' active sites, inhibiting catalytic activity, while ultrasound irradiation disrupts this shielding to restore enzymatic function [26]. These stimuli-responsive properties allow nanozymes to achieve precise control over catalytic processes, facilitating well-regulated sequential reactions.

Although stimuli-responsive nanozymes have enabled external control over catalytic activity, most reported systems still rely either on a single stimulus regulating only one catalytic step [27] or compartmentalize different catalysts without incorporating distinct stimulus-responsiveness [28–30]. As a result, platforms that compartmentalize multiple nanozymes with different stimulus-responsiveness for programmable, stepwise sequential reactions remain largely unexplored.

In this work, we developed a pH-responsive hydrogel bead system using coaxial microfluidic electrospray to spatially compartmentalize GOx-like Au NPs and POD-like Fe_3O_4 NPs. By leveraging the spatial separation and distinct pH-dependent activities of these nanozymes, the system enables stepwise activation of catalytic reactions while minimizing mutual interference. Our results indicate that spatial compartmentalization facilitates sequential activation of nanozyme reactions, suggesting its potential in designing stimuli-responsive cascade systems.

2. Experimental section

2.1. Materials

D-(+)-glucose, 2,2′-azino-bis (3-ethylbenzothiazoline-6-sulfonic acid) diammonium salt (ABTS), sodium borohydride ($NaBH_4$), iron(II) sulfate heptahydrate ($FeCl_2{\cdot}7H_2O$), Fluorescein isothiocyanate–dextran (FITC-Dextran, 59–77 kDa), Rhodamine B isothiocyanate-dextran (RITC-Dextran, 70 kDa) and cobalt(II) sulfate heptahydrate ($CoSO_4{\cdot}7H_2O$) were all purchased from Sigma-Aldrich. Gold(III) chloride trihydrate ($HAuCl_4$) and potassium bicarbonate ($KHCO_3$) were obtained from AK Scientific. Sodium alginate (Na-Alg, molecular weight range 116–227 kDa) was sourced from Duchefa Biochemie. Calcium chloride dihydrate ($CaCl_2{\cdot}2H_2O$) and hydrogen peroxide (H_2O_2, 30 % *w*/w) were acquired from Scharlau. Trisodium citrate (Na_3Cit) was obtained from Laberv. Iron(III) chloride ($FeCl_3$) was supplied by ECP Ltd. Ammonium hydroxide ($NH_4{\cdot}OH$, 28.0–30.0 %) was purchased from Macron Fine Chemicals. Nitric acid (HNO_3, 69.0–70.0 %) was procured from J.T. Baker. Tert-butyl alcohol (TBA) was purchased from Rankem.

2.2. Preparation of Au NPs and Fe_3O_4 NPs

Citrate-capped Au NPs were synthesized following a reported method with a slight modification [31]. A 20 mL aqueous solution containing 1 mM $HAuCl_4$ and 1 mM Na_3Cit was prepared. Subsequently, 0.6 mL of freshly prepared ice-cold 0.1 M $NaBH_4$ was rapidly added under vigorous stirring at room temperature. The reaction mixture turned wine red, indicating the formation of Au NPs. Stirring was continued for 5 min, after which the solution was kept at room temperature for 3 h to allow the excess $NaBH_4$ to fully decompose. The resulting Au NP solution was then stored at 4 °C for further use.

Citrate-modified Fe_3O_4 NPs were prepared using a co-precipitation method with slight modifications [32]. First, 8.3 mmol of $FeCl_3$ and 4.05 mmol of $FeCl_2{\cdot}4H_2O$ were dissolved in 40 mL of DI water at room temperature. The solution was degassed with N_2 for 30 min to remove dissolved O_2. Next, 5 mL of $NH_4{\cdot}OH$ was added dropwise under stirring for 5 min. The mixture was then heated to 90 °C and maintained for 1 h. After cooling to room temperature, the Fe_3O_4 NPs were magnetically separated and washed several times. To functionalize the Fe_3O_4 NPs with citrate, the NPs were first treated with 30 mL of 2 M HNO_3 for 5 min, followed by washing. Then, 30 mL of 0.5 M Na_3Cit solution was added, and the mixture was stirred overnight at room temperature. Finally, the citrate-modified Fe_3O_4 NPs were washed thoroughly and stored at 4 °C.

2.3. Preparation of single and compartmentalized Alg@NPs beads

Single Alg@NPs beads were fabricated using a microfluidic electrospray setup equipped with a stainless-steel blunt syringe needle (outer diameter: 0.31 mm, inner diameter: 0.16 mm). Alg@Au beads were made by mixing 0.1 mL of 5 % (*w*/w) Na-Alg solution with 0.9 mL Au NPs, while Alg@Fe_3O_4 beads were made by combining 0.1 mL of 5 % (*w*/w) Na-Alg solution, 0.9 mL of DI H_2O and 0.23 mg of Fe_3O_4 NPs. Co-loaded Alg@Au/Fe_3O_4 beads, which contain both Au and Fe_3O_4 NPs within a single matrix, were produced by mixing 0.1 mL of 5 % (w/w) Na-Alg solution, 0.9 mL of Au NPs and 0.23 mg of Fe_3O_4 NPs. Each solution was injected at a flow rate of 500 μL/min with a 4 kV high voltage (Spellman's Bertan, Series 230) applied between the needle as the positive electrode and a 0.5 % *w*/*v* $CaCl_2$ aqueous bath as a negative electrode. The needle-to-bath distance was set at 5 cm. To account for the water introduced by the hydrogel beads during catalysis, the embedded water content was estimated based on freeze-drying analysis. Specifically, Alg@Au beads batch contributed 0.53 mL of water per reaction, while the Alg@Fe_3O_4 beads contributed about 0.6 mL (Fig. S1).

For the fabrication of compartmentalized hydrogel beads containing spatially separated nanozymes, a microfluidic electrospray setup with two tapered coaxial capillaries (0.4 mm and 0.2 mm orifices, sourced from Harvard Apparatus) were used, integrated into a T-shaped plastic connector. Alg@Fe_3O_4 beads, in which Fe_3O_4 NPs were confined to the inner domain, were produced with an outer phase of 0.1 mL of 5 % (*w*/w) alginate and 0.9 mL of DI water, and an inner phase consisting of 0.02 mL of 5 % (*w*/w) alginate, 0.18 mL of DI water and 0.23 mg of Fe_3O_4 NPs. Alg@Au beads, in which Au NPs were confined to the outer domain, were prepared with an outer phase of 0.1 mL of 5 % (w/w) alginate and 0.9 mL of Au NPs, and an inner phase containing 0.02 mL of 5 % (*w*/w) alginate and 0.18 mL of DI water. Alg@Au/Fe_3O_4 beads, in which Au NPs were confined to the outer domain and Fe_3O_4 NPs were confined to the inner domain, were made with an outer phase of 0.1 mL of 5 % (*w*/w) alginate and 0.9 mL of Au NPs, and an inner phase consisting of 0.02 mL of 5 % (w/w) alginate, 0.18 mL of DI water, and 0.23 mg of Fe_3O_4 NPs. The inner phase was injected through the inner capillary at 100 μL/min, while the outer phase was introduced through the outer capillary at 500 μL/min. A 4 kV high voltage was applied between the needle and the electrode in the 0.5 % *w*/*v* $CaCl_2$ water bath, with a needle-to-bath distance of 5 cm.

2.4. Detection of catalytic performance of Au and Fe_3O_4 NPs

The GOx-like activity of Au NPs was evaluated using a Co/CO_3 UV–vis assay to quantify the production of H_2O_2 [33]. In a typical procedure, 0.9 mL of 1 M $KHCO_3$ solution was added to a 4 mL vial, followed by 50 μL of 0.07 M $CoSO_4{\cdot}7H_2O$. The mixture was pre-incubated for 10 min to ensure uniform mixing. Then, a 50 μL reaction mixture was introduced, followed by an additional 1 mL of 1 M $KHCO_3$. After 10 min of incubation, the solution was transferred to a quartz cuvette, and the absorbance was initially monitored at 257 nm using UV–Vis spectroscopy.

To evaluate pH-dependent catalytic performance, buffer systems from pH 2 to 9 were applied. Specifically, 0.1 M KCl-HCl for pH 2, 0.1 M acetate buffer for pH 3 to 6 and 0.1 M Tris-HCl buffer for pH 7 to 9. As shown in Fig. S2, H_2O_2 exhibits reduced stability under alkaline conditions (pH 7–9), leading to a decrease in peak absorbance from 0.52 to 0.40. Moreover, a blue shift in the maximum absorbance wavelength was observed from 257 nm at pH 2–6 to 250 nm at pH 7–9. Based on these results, subsequent measurements were performed at 257 nm for pH 2–6 and at 250 nm for pH 7–9 to ensure accurate quantification.

The POD-like catalytic activity of Fe_3O_4 NPs was measured by

monitoring the colorimetric oxidation of ABTS in the presence of H_2O_2. Specifically, 0.23 mg of Fe_3O_4 NPs was dispersed in 2 mL of pH buffer solution, followed by the addition of 0.6 mL DI H_2O, 30 μL of 98 mM H_2O_2 and 30 μL 10 mM ABTS solution. The reaction progress was monitored by measuring the absorbance of $ABTS_{ox}$ at 734 nm using UV–Vis.

To identify the free radicals in the POD-like reaction step, radical scavenger tests were performed (Fig. S3). Alg@Fe_3O_4 beads, prepared form 1 mL of 0.5 wt% Alg and 23 μg Fe_3O_4, were placed in 2 mL of pH 2 buffer with 20 μL of 10 mM ABTS and 20 μL of a H_2O_2. The absorbance at 734 nm of the supernatant of that system (Alg@Fe_3O_4, ABTS, and H_2O_2) reached 1.3 after 10 min. Without Fe_3O_4, ABTS and H_2O_2 system reached only about 0.6 after 10 min, indicating that self-oxidation of ABTS occurs at pH 2. Without H_2O_2, the absorbance was nearly zero, confirming that the reaction is H_2O_2-dependent. TBA was then added as a selective scavenger of the ·OH radical [34]. TBA at 0.50 to 1.0 M strongly suppressed the reaction rate to the no-catalyst baseline, whereas 0.25 M had little effect. These results indicate that ·OH radicals are the dominant oxidant in the Fe_3O_4-mediated peroxidase-like step at pH 2.

2.5. Characterization

The images of the hydrogel beads were obtained by bright-field and fluorescence microscopy using an inverted biological microscope (MI52-N, Micro-shot Technology) equipped with an LED fluorescence illuminator (MI-BYU-LED, Micro-shot Technology). UV–Vis spectrophotometry (NanoPhotometer® NP80) was used to measure the absorbance of the $Co(CO_3)_3^{3-}$ complex and oxidized ABTS, thereby evaluating the catalytic activity of the Au and Fe_3O_4 nanozymes. X-ray diffraction (XRD) patterns were recorded using a Rigaku MiniFlex II diffractometer, which scanned over a 2θ range of 5–90° at 0.02° step intervals. The surface morphology and elemental distribution were examined using scanning electron microscopy (SEM, Gemini). Elemental analysis was performed by inductively coupled plasma triple-quadrupole mass spectrometry (ICP-QQQ-MS, Agilent 8900) operated in He mode to minimize polyatomic interferences. Transmission electron microscopy (TEM, FEI Tecnai F20, Philips) was employed to determine the size and

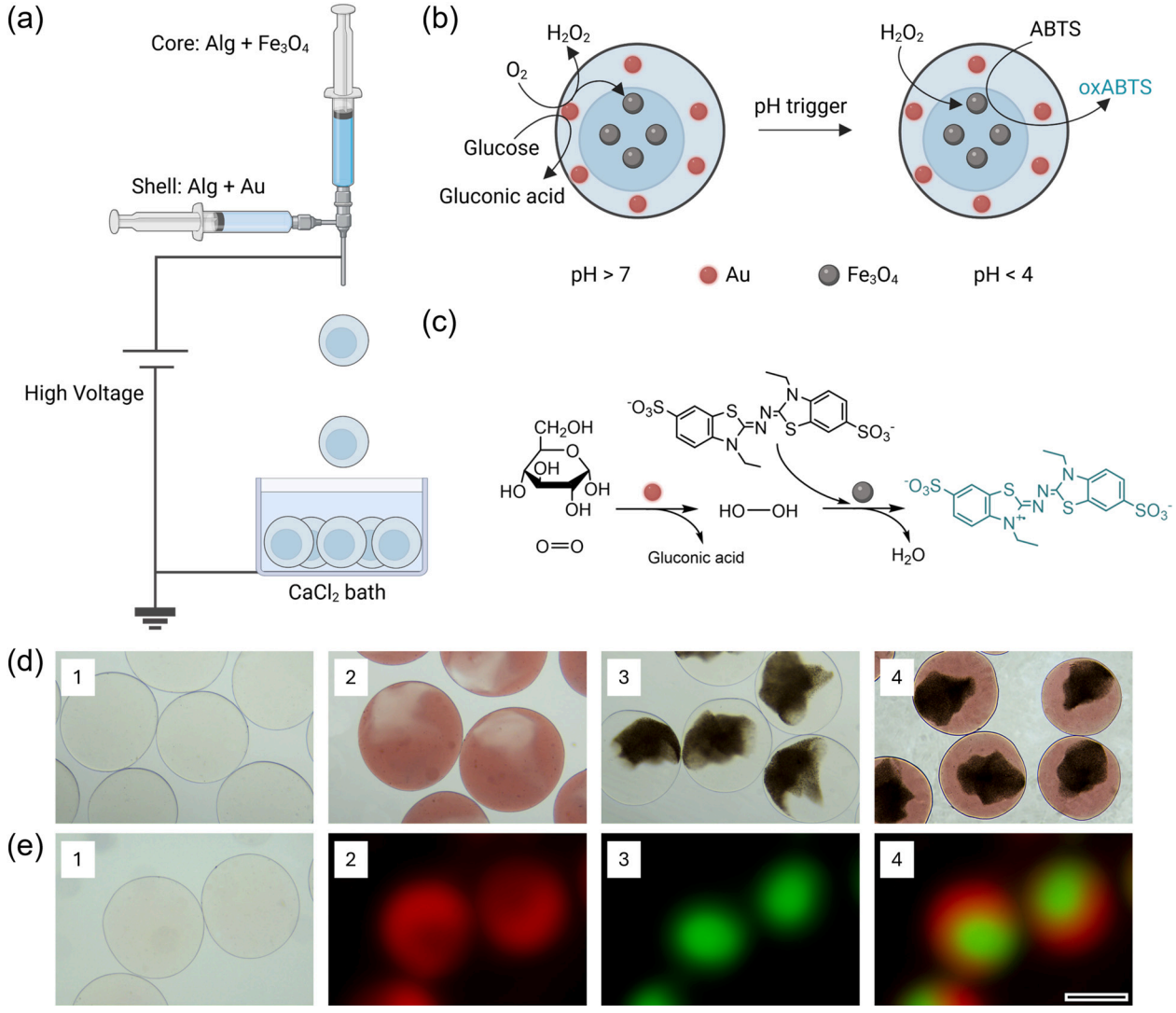

Fig. 1. (a) Schematic of the electrospray microfluidic system for fabricating compartmentalized Alg@Au/Fe_3O_4 beads utilising ionic crosslinking in a $CaCl_2$ bath. (b) pH-responsive sequential reaction: Au NPs catalyse glucose oxidation under alkaline conditions (pH > 7), producing H_2O_2; Fe_3O_4 NPs are activated under acidic conditions (pH < 4) to oxidize ABTS to blue $ABTS_{ox}$. (c) Reaction scheme illustrating the Au and Fe_3O_4 nanozymes-mediated processes. (d) Bright-field microscopic images of various hydrogel bead compositions:1: blank alginate beads; 2: Alg@Au beads; 3: Alg@Fe_3O_4 beads; 4: Alg@Au/Fe_3O_4 beads. (e) Fluorescence images of the compartmentalized hydrogel beads. 1: Bright-field image; 2: Yellow channel fluorescence; 3: Blue channel fluorescence; 4: Merged image showing spatial separation of compartments. Scale bar: 1000 μm.

morphology of the synthesized Au and Fe_3O_4 NPs. All quantitative data presented in this study were obtained from $n = 3$ independent experiments. Error bars in all figures represent the mean ± standard deviation (SD) of the stated n.

3. Results and discussion

3.1. System design and fabrication of the Alg compartmentalized beads

We designed compartmentalized hydrogel beads incorporating Au and Fe_3O_4 NPs to control sequential reactions triggered by pH stimuli. As illustrated in Fig. 1a, the beads were fabricated using a microfluidic electrospray system equipped with a coaxial nozzle. The outer solution, loaded with Au NPs, and the inner solution, containing Fe_3O_4 NPs, were co-injected and rapidly crosslinked in a $CaCl_2$ bath, resulting in the formation of monodisperse hydrogel beads. Under alkaline conditions (pH > 7), the Au-rich outer compartment catalyse glucose oxidation, generating H_2O_2, which diffused into the Fe_3O_4-rich inner compartment and surrounding solution (Fig. 1b, left). This process was quantified using a cobalt–carbonate assay and monitored by UV–Vis absorbance at 257 nm [35]. Upon acidification (pH < 4), the Fe_3O_4-rich inner compartment becomes catalytically active, initiating a Fenton-like reaction that decomposes H_2O_2 into ROS [36–39] which in turn oxidize ABTS to generate a distinct blue $ABTS_{ox}$ (Fig. 1b, right). The molecular basis of this dual-step sequential process is illustrated in Fig. 1c, showing the Au-mediated glucose oxidation and subsequent Fe_3O_4-catalyzed ABTS oxidation. By using the spatial separation of Au and Fe_3O_4 NPs within the compartmentalized hydrogel structure, and their distinct pH-responsive catalytic behaviours, we demonstrate a controllable sequential reaction system triggered by pH.

The successful formation of the spatially compartmentalized structure was confirmed by bright field and fluorescence imaging, as shown in Fig. 1d and e. Bright field images demonstrate that Au and Fe_3O_4 NPs can be individually loaded within hydrogel beads, while the compartmentalized beads display both components without observable mixing. Fluorescence microscopy provides direct evidence for spatial segregation: the yellow channel (Fig. 1e2) shows RITC-dextran dyes restricted to the outer region, while the blue channel (Fig. 1e3) highlights FITC-dextran dyes confined to the inner region. The merged image (Fig. 1e4) reveals a distinct compartmental boundary with minimal overlap, demonstrating the effective spatial separation of the two fluorescence dyes. This compartmentalization is achieved and maintained through the microfluidic coaxial electrospray process, in which the outer and inner solutions, each containing only one type of NPs, are rapidly and separately crosslinked upon contact with Ca^{2+} ions. The rapid gelation kinetics, which are much faster than NPs diffusion, physically lock the Au and Fe_3O_4 NPs within their respective compartments. The resulting hydrogel matrix serves as an effective barrier, preserving the compartmentalized architecture throughout subsequent experiments.

3.2. Catalytic performance of Au NPs in solution and Alg@Au beads at different pH

Au NPs exhibit strong GOx-like activity but are prone to instability and aggregation due to variations in solution parameters, such as pH and ionic strength [40,41]. To address this, we encapsulated Au NPs within Alg beads, a naturally derived biopolymer that readily forms a three-dimensional cross-linked structure upon ionic crosslinking with Ca^{2+}. The porous network allows the diffusion of small molecules toward the Au NPs' surface, enabling efficient access to catalytically active sites. Here, we first examine the time-dependent GOx-like activity of 'free' Au NPs in solution and Alg@Au beads across a pH range of 2 to 9, focusing on the influence of pH on catalytic performance and reaction kinetics.

The morphology and distribution of the synthesized Au NPs were characterized by TEM, as shown in Fig. S4a. When encapsulated in Alg@Au beads (Fig. S4b), the Au NPs remain relatively well dispersed within the hydrogel matrix. Size distribution analysis (Fig. S4c) indicates an average diameter of 6 ± 1 nm, with a coefficient of variation (CV) of 19 %. UV–Vis absorbance spectroscopy (Fig. S4d) shows an absorbance of 0.969 at 450 nm and a surface plasmon resonance (SPR) peak at 511 nm with an absorbance of 1.236. According to calculations based on the method by Haiss et al. [42], the absorbance ratio (A_{450}/A_{511}) corresponds to an average particle diameter of 5 nm, which is reasonably consistent with the TEM results. The corresponding mass concentration of Au NPs was calculated to be 2.04 μg/mL.

Fig. 2a illustrates the GOx activity of free Au NPs over 1 h across a pH range of 2 to 9. The reaction system consisted of 0.9 mL of Au NP solution, 0.2 mL of 1 M glucose, and 1.43 mL of pH buffer. All reactions were conducted under O_2-rich conditions maintained by continuous bubbling of O_2. To verify the essential role of O_2, we compared free Au NPs' catalytic activity under N_2, air and O_2 atmospheres at pH 9 (Fig. S5). The activity was significantly enhanced under O_2, while it was minimal in N_2, confirming the dependence of the reaction on O_2. Under alkaline conditions of pH 9, the reaction proceeded most efficiently, with absorbance rapidly increasing and reaching 0.78 after 60 min. Moderate activity was observed at pH 8 and 6, where absorbance values plateaued around 0.45 within 20 min. The catalytic efficiency was notably lower at pH 4, 5 and 7, with absorbance stabilising around 0.2 within 20 min. There was minimal to no catalytic activity under pH 2 and 3, where absorbance remained close to zero throughout the experiment.

The reaction mixture for the Alg@Au system consisted of Alg@Au beads, 1.8 mL of pH buffer and 0.2 mL of 1 M glucose. For a control experiment, the Alg@Au beads were replaced with plain Alg beads under otherwise identical conditions. Fig. 2b displays the GOx-like activity of Alg@Au beads over 6 h across a range of pH conditions. At pH 9, the absorbance increased steadily, reaching approximately 0.75 at 6 h. At pH 8, the reaction progressed efficiently, with the absorbance plateauing around 0.55. A moderate increase was observed at pH 7, where the absorbance reached 0.2. In contrast, negligible absorbance was observed under acidic to neutral conditions of pH 2–6 throughout the entire reaction period. Control experiments using plain alginate beads exhibited no detectable absorbance across the pH range of 2 to 9, confirming that the observed catalytic activity was exclusively attributed to the presence of Au NPs (as shown in Fig. S6).

Both 'free' Au NPs and Alg@Au beads exhibit pH-dependent GOx-like activity, with higher catalytic efficiency observed at alkaline pH. We measured the pH values before and after the reactions to assess whether the catalytic process alters the bulk solution pH. As shown in Fig. S7, both systems showed minimal pH variation across the entire pH range, with ΔpH values remaining within ±0.3 under all pH conditions. These results indicate that the glucose oxidation reactions occurred under stable pH conditions, even though the reaction rate depends on the solution pH [43]. The observed pH-dependence is primarily attributed to the role of hydroxide ions (OH^-), which act as Brønsted bases to facilitate glucose dehydrogenation by activating the hydroxyl group at the C1 position. This activation leads to the formation of a hydrated glucose anion on the Au surface, which subsequently initiates a nucleophilic attack on O_2 [44–46]. Importantly, as illustrated in Fig. 2c, this process follows a selective $2e^-$ transfer pathway, wherein the Au NPs catalyse glucose oxidation while simultaneously reducing O_2 to H_2O_2. This $2e^-$ reduction avoids O—O bond cleavage and favours H_2O_2 formation over complete reduction to water [44,47]. The produced H_2O_2 subsequently reacts with Co^{2+} in the presence of bicarbonate (HCO_3^-), forming a cobalt–carbonate complex, $Co(CO_3)_3^{3-}$, which exhibits a strong absorbance at 257 nm [33].

Although both free Au NPs and Alg@Au beads exhibit pH-dependent GOx-like activity, their reaction kinetics differed markedly. As shown in Fig. 2d, the initial reaction rates were calculated based on H_2O_2 concentration using a standard calibration curve (Fig. S8), using absorbance measurements over the first 10 min of free Au NPs and the first 1 h for Alg@Au beads. Free Au NPs exhibited significantly higher catalytic

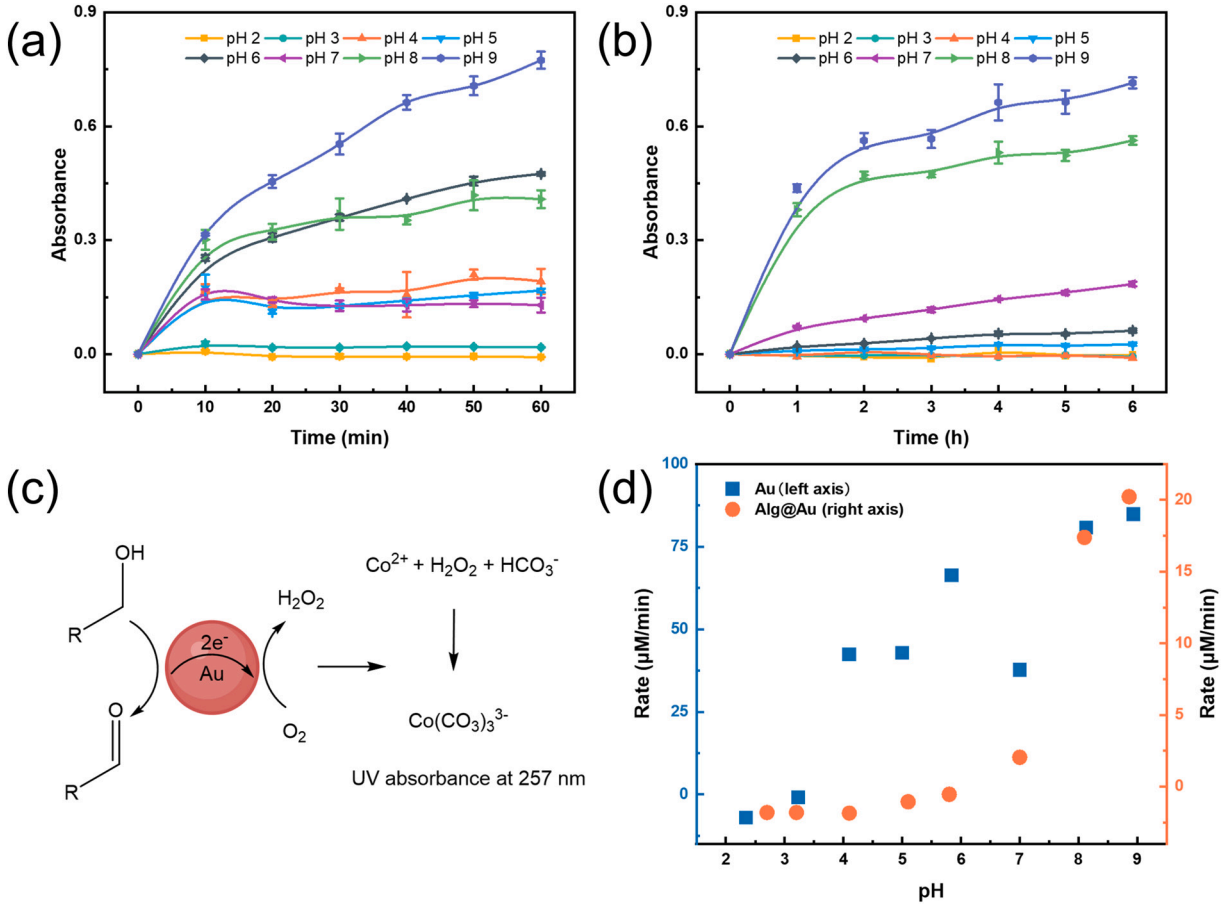

Fig. 2. Time-dependent absorbance profiles show GOx-like activity at various pH levels for (a) Au NPs in solution over 1 h and (b) Alg@Au beads over 6 h. (c) Mechanism of Au-catalyzed glucose oxidation and subsequent Co^{2+} detection. (d) Initial reaction rates (μM/min) of H_2O_2 production as a function of pH for free Au NPs in solution at 10 min (left axis) and Alg@Au beads at 1 h (right axis).

efficiency, with reaction rates increasing from 40 μM/min at pH 4–5 to 66 μM/min at pH 6, 80 μM/min at pH 8 and peaking at 84 μM/min at pH 9. Notably, the rate at pH 7 (38 μM/min) was unexpectedly lower than at pH 6, suggesting that factors beyond pH, such as buffer composition and ionic strength, may influence catalytic activity, in line with reports showing that buffer types and salt concentration can modulate nanozyme performance through electrostatic and coordination interactions [48]. The buffer system shifted from 0.1 M KCl–HCl at pH 2, to 0.1 M acetate buffer between pH 3–6 and to 0.1 M Tris–HCl from pH 7–9, which may partially account for the non-linear changes in reaction rates. In contrast, Alg@Au beads followed a similar pH-dependent trend but exhibited consistently lower reaction rates across the entire pH range. The rate was negligible below pH 6, then gradually increased to 2.0 μM/min at pH 7, followed by a rise to 17.4 μM/min at pH 8, reaching a maximum of 20 μM/min at pH 9. The Alg@Au displayed a stable increase in catalytic activity with rising pH, suggesting that the hydrogel network helps maintain a stable local environment, protecting the catalytic process from fluctuations in bulk pH or ionic strength [49].

To better interpret the catalytic behaviour of Au-based systems, time-dependent absorbance data were fitted using pseudo-first order (PFO) [50] and pseudo-second order (PSO) [51] kinetic models (Fig. S9, Table S1–S2). Although initially developed to describe adsorption kinetics [52], the PFO and PSO models have since been widely applied to surface-mediated processes, including enzyme-like nanozyme catalysis [53,54]. Continuous O_2 bubbling was employed to ensure oxygen saturation, thereby allowing the reaction to be analyzed assuming that O_2 concentration remained constant and non-limiting. Since H_2O_2 generation was negligible under acidic and neutral conditions (pH 2–7), kinetic analysis was restricted to pH 8 and 9. The results showed that for free Au NPs and Alg@Au hydrogel beads, the PSO model consistently yielded higher R^2 values than the PFO model [55]. Notably, at pH 9, PSO kinetic analysis gave $k = 0.062\ min^{-1}$ ($R^2 = 0.995$) for free AuNPs and $k = 0.021\ min^{-1}$ ($R^2 = 0.990$) for Alg@Au beads, confirming the diffusion limitation in hydrogel systems. The alginate network imposes a diffusional barrier that limits the transport of glucose and O_2, while partial encapsulation may obstruct access to active catalytic sites, collectively reducing reaction efficiency. An additional Michaelis–Menten kinetic analysis was explicitly conducted for free Au NPs at pH 9 using varying glucose concentrations to evaluate the intrinsic catalytic properties further. The resulting Lineweaver–Burk plot (Fig. S10) showed good linearity, yielding an apparent V_{max} of 0.284 min^{-1} and a K_m of 11.5 mM, consistent with high substrate affinity and typical GOx-like activity in alkaline media [56,57].

3.3. *Catalytic performance of 'Free' Fe_3O_4 and Alg@Fe_3O_4 beads at different pH*

This section investigates the time-dependent POD-like activity of free Fe_3O_4 NPs and Alg@Fe_3O_4 beads across a pH range of 2 to 9, focusing on the influence of pH on catalytic performance and reaction kinetics. XRD patterns of Fe_3O_4 NPs before and after rinsing in 2 M HNO_3 (Fig. S11a) show the same diffraction peaks at 30.1° (220), 35.5° (311), 43.3° (400), 57.0° (511), and 62.6° (440), with a difference of some increase in the amorphous background at 15–25° for the rinsed NPs. This is consistent with a slight surface etching, rather than a phase transformation. The TEM image (Fig. S11b) shows near-spherical, well-dispersed particles,

while the size analysis (Fig. S11c) yields an average diameter of 14 ± 3 nm (CV 22 %). When encapsulated in alginate (Fig. S11d), the Fe_3O_4 NPs remain uniformly distributed within the hydrogel matrix without large aggregates.

The reaction mixtures for Fe_3O_4 NPs in solution were prepared by dispersing 0.23 mg of Fe_3O_4 NPs in 2 mL of pH buffer, followed by the addition of 0.6 mL DI H_2O, 30 μL of 98 mM H_2O_2, and 30 μL of 10 mM ABTS solution. Fig. 3a shows the time-dependent POD-like activity of free Fe_3O_4 NPs over 3 h, demonstrating a strong pH dependency. At pH 2, Fe_3O_4 exhibited the highest catalytic activity, with absorbance rapidly increasing to approximately 1.5 within 30 min and remaining stable throughout the reaction. At pH 3, the absorbance rapidly increased to 0.42 within 30 min and then gradually increased to around 0.6 after 180 min. At pH 4, only slight increases in absorbance were observed, with final values of less than 0.2. In contrast, negligible catalytic activity was detected at pH 5 to 9, where the absorbance remained nearly zero throughout the measurement period.

The reaction mixture for Alg@Fe_3O_4 beads included the Alg@Fe_3O_4 beads, 30 μL of 10 mM ABTS, 30 μL of 98 mM H_2O_2 and 2 mL of buffer solutions. Two types of control experiments were conducted under the identical conditions: one using plain Alg beads with both ABTS and H_2O_2 and another using plain Alg beads with ABTS only. Fig. 3b presents the time-dependent catalytic activity of Alg@Fe_3O_4 beads over 3 h under varying pH conditions. At pH 2, the highest activity was observed, with the absorbance continuously rising to approximately 1.0 by 180 min. Moderate activity was detected at pH 3 and 4, where absorbance reached 0.44 and 0.16, respectively. Across pH 5 to 9, the catalytic activity was negligible, with absorbance remaining close to zero throughout the experiment. Fig. S12a shows the time-dependent absorbance profiles of plain Alg beads in the presence of ABTS and H_2O_2. A notable increase in absorbance was observed under acidic conditions, reaching approximately 0.42 at pH 2 and 0.1 at pH 3, while minimal changes were detected from pH 4 to 9. This suggests that ABTS can undergo non-catalytic oxidation in the presence of H_2O_2 under strongly acidic conditions. In contrast, Fig. S12b presents plain Alg beads with ABTS only, where the absorbance remained near zero across all pH values, confirming that H_2O_2 is essential for initiating ABTS oxidation.

Both free Fe_3O_4 NPs and Alg@Fe_3O_4 beads exhibit pH-dependent POD-like activity. We measured the pH values before and after the reaction to assess whether the catalytic process alters the bulk solution pH. As shown in Fig. S13, both systems showed minimal pH variation across the entire pH range, with ΔpH values remaining within ±0.15. These results confirm that the POD-like reactions occurred under stable pH conditions, allowing accurate evaluation of pH-dependent catalytic performance without interference from buffer drift. Their catalytic activity follows a Fenton-like reaction mechanism, as illustrated in Fig. 3c. In this process, H_2O_2 absorbed on the surface of Fe_3O_4 NPs accepts electrons from Fe^{2+} ions to produce ROS, which oxidize ABTS to its blue-colored $ABTS_{ox}$. Radical-scavenging experiments with Alg@Fe_3O_4 beads demonstrated that the H_2O_2-dependent POD-like reaction proceeds *via* ·OH radicals as the dominant oxidant at pH 2. Meanwhile, electron transfer through Fe^{2+}-O-Fe^{3+} chains regenerates active Fe^{2+} sites, thereby sustaining the catalytic cycle [58]. Additionally, under acidic conditions, iron remains soluble in its ferric or ferrous form, which supports catalytic activity. H_2O_2 also remains stable and resists premature decomposition [59]. In contrast, at neutral and alkaline conditions, Fe ions tend to precipitate as Fe hydroxide/oxides, reducing the

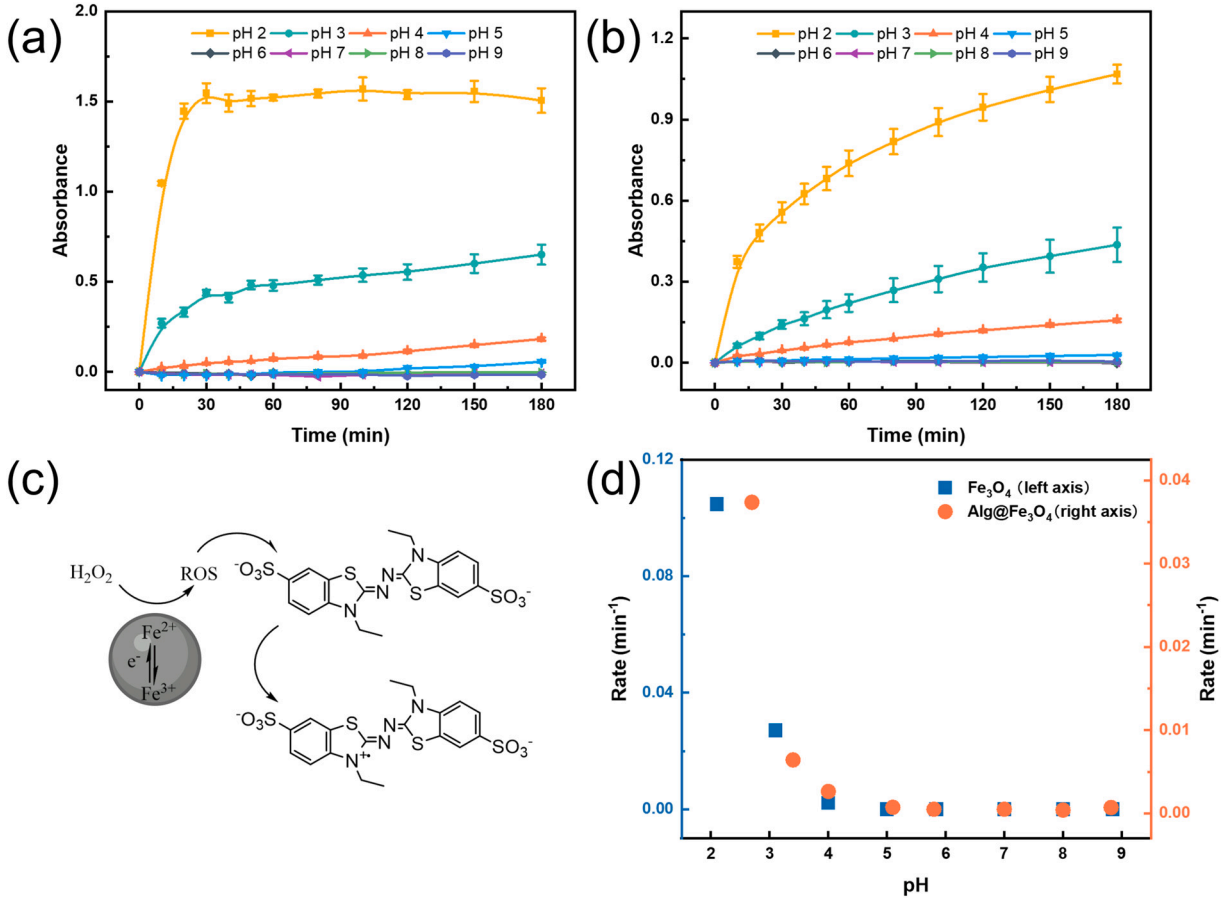

Fig. 3. Time-dependent absorbance profiles for POD-like activity of free Fe_3O_4 NPs (a) and Alg@Fe_3O_4 beads (b) at various pH levels over 3 h. (c) Mechanism of the Fe_3O_4-catalyzed peroxidase-like reaction. Fe^{2+}/Fe^{3+} valence cycling promotes the decomposition of H_2O_2 into ROS, which subsequently oxidize ABTS into its colored radical product. (d) Initial reaction rates (min^{-1}) of H_2O_2 production as a function of pH for free Fe_3O_4 NPs (left axis) and Alg@Fe_3O_4 beads at 10 min.

availability of active redox sites [60]. Moreover, H_2O_2 decomposes more readily into water and O_2 [61], further limiting ROS generation. These factors account for the superior catalytic activity observed under acidic conditions.

Although free Fe_3O_4 NPs and Alg@Fe_3O_4 beads exhibit pH-dependent POD-like activity, their reaction kinetics differed significantly. As shown in Fig. 3d, the initial reaction rates were estimated from the slope of the absorbance increase at 734 nm over the first 10 min, during which the reaction showed linearity. Since the absorbance could not be converted to concentration, it was used as a proxy for the concentration of the oxidized species, and the rates were expressed in min^{-1}. Free Fe_3O_4 NPs displayed their highest catalytic rate at pH 2, reaching 0.105 min^{-1}, sharply decreasing to 0.027 min^{-1} at pH 3 and dropping further to 0.0022 min^{-1} at pH 4. Beyond pH 5, the activity became negligible. The Alg@Fe_3O_4 beads also followed a similar pH-dependent trend, although with a uniformly lower activity across all pH values. At pH 2.7, the initial rate was 0.037 min^{-1}, at pH 3.4 the rate was 0.0064 min^{-1}, declining further to 0.0026 min^{-1} at pH 4. Above pH 5, the reaction did not proceed. The reduced activity in the Alg@Fe_3O_4 system is partly attributed to the presence of alginate, whose carboxyl and hydroxyl groups consume protons in acidic environments due to partial protonation, thereby increasing the local pH [62,63]. This local pH increase weakens the Fenton-like reactivity of Fe_3O_4 under strongly acidic conditions.

To further investigate the reaction mechanism of Fe_3O_4-based catalytic systems, time-dependent absorbance data were fitted to PFO and PSO kinetic models (Fig. S14, Tables S3–S4). As significant catalytic activity was only observed under acidic conditions, kinetic analysis was conducted at pH 2 and 3. Both free Fe_3O_4 NPs and Alg@Fe_3O_4 beads yielded consistently good linear fits only with the PSO model, suggesting that the reaction is governed by surface interactions and diffusion-controlled processes [64–66]. Notably, at pH 2, PSO kinetic analysis gave $k = 0.490$ min^{-1} ($R^2 = 0.998$) for free Fe_3O_4 NPs and $k = 0.023$ min^{-1} ($R^2 = 0.989$) for Alg@Fe_3O_4 beads, suggesting the diffusion limitation in hydrogel systems. Specifically, hydrogel encapsulation may restrict H_2O_2 and ABTS diffusion and partially shield the Fe-active sites, thereby reducing the overall catalytic performance. To further evaluate the intrinsic activity of free Fe_3O_4 NPs, Michaelis–Menten kinetic analysis was conducted under pH 2 using varying H_2O_2 concentrations. The resulting Lineweaver–Burk plot (Fig. S15) showed good linearity, yielding an apparent V_{max} of 0.724 min^{-1} and a K_m of 0.308 mM, which reflects a high catalytic efficiency and strong substrate affinity under acidic conditions [23].

3.4. pH-controlled sequential reaction using au and Fe_3O_4 NPs

To study the impact of the catalysts' composition and spatial distribution on sequential reactions, we first evaluated the GOx-like activity in a reaction system containing 1.8 mL of pH 9 Tris–HCl buffer and 0.2 mL of 1 M glucose. For the free nanozyme system (Fig. 4a), Au-only showed the highest activity (absorbance reaching 0.9), whereas the Au/Fe_3O_4 mixture gave a lower response (absorbance reaching 0.8), indicating that Fe_3O_4 partially suppresses Au-catalyzed oxidation. Fe_3O_4 alone and blank buffer were essentially inactive. For the single alginate system (Fig. 4b), encapsulation preserves the same activity order. Alg@Au showed the highest activity (absorbance reaching 0.6), followed by Alg@Au/Fe_3O_4 (absorbance reaching 0.4). The absorbance plateau decreases due to diffusion limitations in the alginate beads. Alg@Fe_3O_4 and Alg can be considered essentially inactive. To further explore the role of spatial arrangement in mitigating potential interference between Au and Fe_3O_4, we examined core-shell bead architectures (Fig. 4c) under the same conditions. Both Alg@Au and Alg@Au/Fe_3O_4 configurations demonstrated comparable catalytic activity, with absorbance increasing to 0.6. Alg@Fe_3O_4 and Alg beads exhibited negligible activity. Moreover, pH remained stable at 9 throughout the reaction for all tested systems (Fig. S16).

We next investigated the POD-like activity in a reaction system composed of 2 mL of pH 2 buffer, 30 μL of 98 mM H_2O_2 and 30 μL of 10 mM ABTS. For the free nanozyme system (Fig. 4d), Fe_3O_4-only produced the fastest and strongest colour development (absorbance reaching 1.3), whereas the Au/Fe_3O_4 mixture was weaker (absorbance reaching 0.9). Au alone and the blank were essentially inactive. For the single alginate system (Fig. 4e), Alg@Fe_3O_4 and Alg@Au/Fe_3O_4 exhibited similar strong catalytic performance, with absorbance at 734 nm increasing to 0.8. Alg@Au and Alg beads showed lower absorbance values of 0.3. To further study the influence of different spatial distributions, we tested core-shell architectures under the same conditions (Fig. 4f). Alg@Fe_3O_4 and Alg@Au/Fe_3O_4 maintained similar high activity, reaching an absorbance of 0.6. Alg@Au and Alg beads showed low activity with an absorbance of 0.2. Moreover, H_2O_2 diffused into both single and core-shell Alg beads (Fig. 4g), with the absorbance at 257 nm dropping from 0.60 to 0.43 within 10 min and remaining stable, confirming that the diffusion effect of H_2O_2 on the kinetics of response is negligible. The pH remained stable throughout the reaction for all bead systems (Fig. S17).

We further analyzed the relative initial reaction rates to compare different formulations. First, Fig. 4h compares the GOx-like initial rates at pH 9. Initial rates were obtained by linear regression of the early linear regime, 10 min for the free catalysts and 60 min for the single and core–shell beads, normalized to the Au-only condition, which was set to 100 %. In the free system, co-present Au/Fe_3O_4 showed a reduced rate (85 %; $^{**}p < 0.001$; Hedges' $g = 3.42$). In the single beads, the inhibition became stronger (60 %; $^{**}p < 0.001$; $g = 18.75$), consistent with co-immobilized Fe_3O_4 suppressing Au-catalyzed oxidation. In contrast, the core–shell architecture essentially removed this inhibition: Au/Fe_3O_4 was comparable to Au (105 %; n.s.; $g = -0.44$). These results indicate that, although co-present Fe_3O_4 can markedly depress Au-driven GOx-like activity in both free and single bead systems, spatial separation of Au and Fe_3O_4 into core-shell architecture largely mitigates interference, yielding initial rates comparable to those of the Au-only control.

Second, Fig. 4i compares the POD-like initial rates at pH 2. Initial rates were obtained from the early linear regime, 10 min for the free catalysts and 60 min for the single and core-shell beads, normalized to the Fe_3O_4-only condition (100 %). For the free system, the Au/Fe_3O_4 mixture was significantly lower than Fe_3O_4 (70 %; $p < 0.001$; Hedges' $g = 16.91$), indicating Au-induced suppression in solution. In the single alginate beads, Au/Fe_3O_4 became slightly higher than Fe_3O_4 (110 %; $p < 0.01$; Hedges' $g = -2.84$). In the core-shell beads, Au/Fe_3O_4 and Fe_3O_4 were similar (100 %; n.s.; Hedges' $g = -1.25$), showing that encapsulation largely buffers the Au/Fe_3O_4 interaction. These data confirm that POD-like is governed by Fe_3O_4, while the effect of Au co-presence is inhibitory only in the free state and becomes negligible once embedded in alginate.

Before performing the sequential reactions under pH control, we confirmed that the pH switch does not damage the beads (Fig. S18). In one cycle, the pH was adjusted from 7 to 9, then to 2, and finally back to 9. The diameter, normalized to the initial value at pH 7, expanded in base, contracted in acid, and recovered upon to 90 % of its original value at pH 9. The zeta potential shifted consistently with alginate carboxylate ionization, from about −22 mV at pH 7 to about −40 mV at pH 9, then to about −12 mV at pH 2, and finally to about −31 mV after the last pH 9 step. Optical micrographs after the cycle show intact beads with preserved core-shell contrast.

For the free nanozyme system (Fig. 5a), the first GOx-like reaction, characterized by an increase in absorbance to 0.6, occurred within 20 min. Following this step, the pH was adjusted to 2, and 30 μL of 10 mM ABTS was added to initiate the POD-like reaction. Over the next 20 min, the absorbance rose sharply to 1.0. The controls confirm that the POD-like reaction did not occur without a pH switch, and the absorbance remained at zero. Au-only but with pH switch produced only a small signal from non-catalytic ABTS self-oxidation by H_2O_2 under acidic

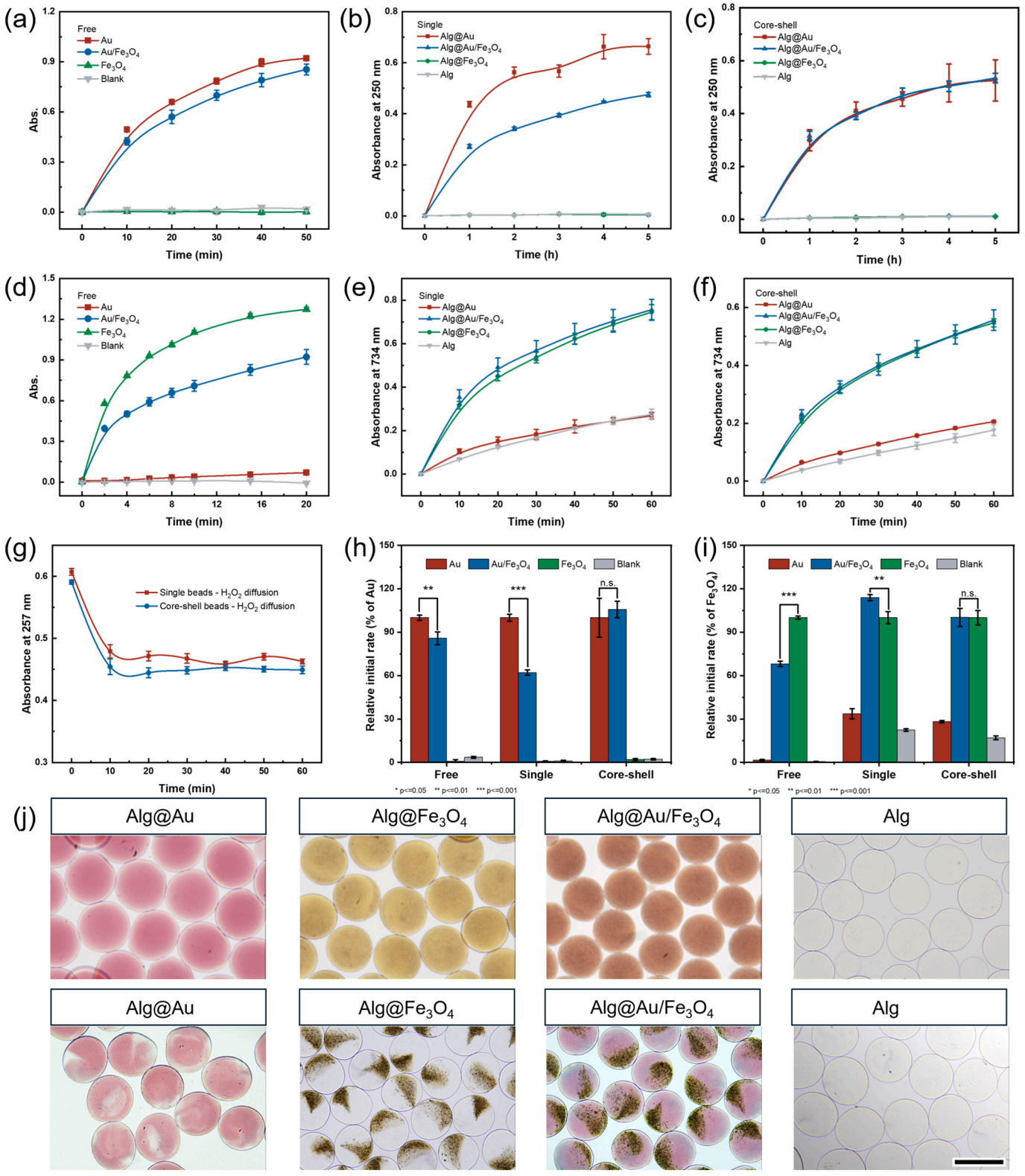

Fig. 4. Time-dependent absorbance profiles for GOx-like activity of (a) free, (b) single, and (c) core-shell beads containing Au, Au/Fe_3O_4, Fe_3O_4, or blank at pH 9. Time-dependent absorbance profiles for POD-like activity of (d) free, (e) single and (f) core-shell beads containing Au, Au/Fe_3O_4, Fe_3O_4 or blank at pH 2. (g) Diffusion of H_2O_2 into single and core-shell alginate beads over 60 min. (h) Relative initial reaction rates (GOx-like) of free, single, and core-shell beads containing Au, Au/Fe_3O_4, Fe_3O_4, or blank at pH 9; (i) relative initial reaction rates (POD-like) free, single, and core-shell beads containing Au, Au/Fe_3O_4, Fe_3O_4, or blank at pH 2. (j) Optical microscopy images of the hydrogel beads, including single (top row) and core-shell (bottom row) Alg beads structures. The scale bar is 500 μm.

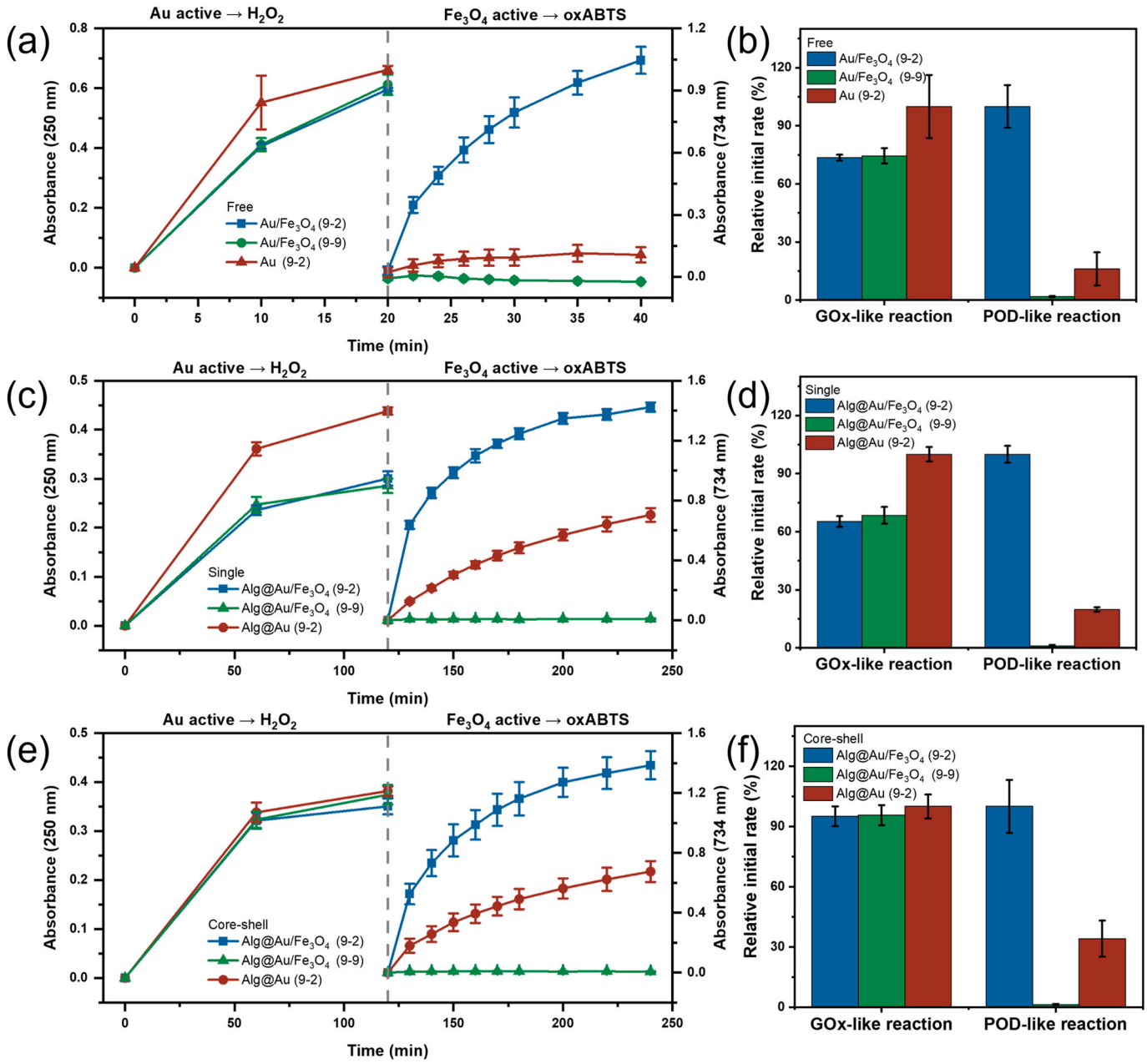

Fig. 5. Time-dependent absorbance profiles at 250 nm (left, GOx-like activity) and 734 nm (right, POD-like activity) illustrating sequential reactions in (a) free, (c) single and (e) core-shell beads. Relative initial reaction rates (GOx-like activity) and (POD-like activity) for (b) free, (d) single and (f) core-shell beads.

conditions. Fig. 5b quantifies the initial rates for the free systems. For the GOx-like step, the Au-only system is taken as 100 % and the Au/Fe_3O_4 formulations reach only 75 %. For the POD-like step, Au/Fe_3O_4 (pH 9 to 2) exhibits the highest rate (set to 100 %), whereas maintaining the pH at 9 reduces the rate to near zero and Au-only (pH 9 to 2) yields only a minor (15 %) response.

We next evaluated the sequential reactions within single beads (Fig. 5c). In GOx-like reactions, Alg@Au reached an absorbance of 0.45, and Alg@Au/Fe_3O_4 showed a lower plateau at an absorbance of 0.3. After the pH switch from 9 to 2, in the POD-like reactions, robust ABTS oxidation occurred only for Alg@Au/Fe_3O_4, while maintaining the pH at 9 produced no signal, and Alg@Au showed a weak increase in absorbance upon the pH was switched. Consistently, the initial rates (Fig. 5d) indicate Alg@Au/Fe_3O_4 retained 60 % of the H_2O_2 generation rate of the Alg@Au in the GOx-like step. For the POD-like reaction, Alg@Au/Fe_3O_4 (pH 9 to 2) was set to 100 %, whereas Alg@Au contributed only 20 % and Alg@Au/Fe_3O_4 (pH 9 to 9) was near zero.

We then evaluated the sequential reactions using core-shell beads. Alg@Au/Fe_3O_4 and Alg@Au show comparable absorbance in the GOx-like reactions in Fig. 5e, indicating that the Au/Fe_3O_4 inhibition observed in free and single bead systems is largely removed by core-shell partitioning. After the pH switch from 9 to 2, robust ABTS oxidation is observed only for Alg@Au/Fe_3O_4, while Alg@Au exhibits only a weak rise and the control of Alg@Au/Fe_3O_4 maintained at pH 9 showed no response. Consistently, Fig. 5f shows that the initial rates of Alg@Au/Fe_3O_4 are comparable to Alg@Au in GOx-like reactions. For the POD-like step, the initial rates of Alg@Au/Fe_3O_4 (pH 9 to 2) are set to 100 %, whereas Alg@Au contributes only 30 %, and the control of Alg@Au/Fe_3O_4 maintained at pH 9 shows nearly zero activity. The pH remained stable throughout the reaction for all bead systems (Fig. S19). Representative photographs of the final reaction mixtures are shown in Fig. S20, which visually confirm the spectroscopic results and highlight

the roles of Au, Fe_3O_4 and pH modulation in the sequential reactions. Furthermore, Fig. S21 demonstrates that the core-shell Alg@Au/Fe_3O_4 beads respond directionally to an external magnetic field, confirming their magnetic responsiveness.

3.5. *Operational stability and logic gated application of core-shell Alg beads*

We evaluated the reusability of core-shell Alg@Au/Fe_3O_4 beads by using them under a programmed pH switch and performing five cycles. Each cycle consisted of a GOx-like reaction at pH 9, followed by a POD-like reaction at pH 2. Between cycles, the beads were thoroughly rinsed and re-crosslinked in 2 % $CaCl_2$ for 30 min to restore the stabilization of the Alg beads. Reaction activities were normalized to the first use, with cycle 1 set at 100 % (Fig. 6a). The GOx-like absorbance ratio decreased to 30 % in cycle 2 and then decreased more gradually to 20 % by cycle 5. A likely reason for that decrease is the swelling/deswelling of the beads when the pH is switched (Fig. S18) where the Au NP may be expelled from the beads during the first cycle. The POD-like step was less affected, with ratios of 90 % in cycle 3 and 55 % in cycle 5. We

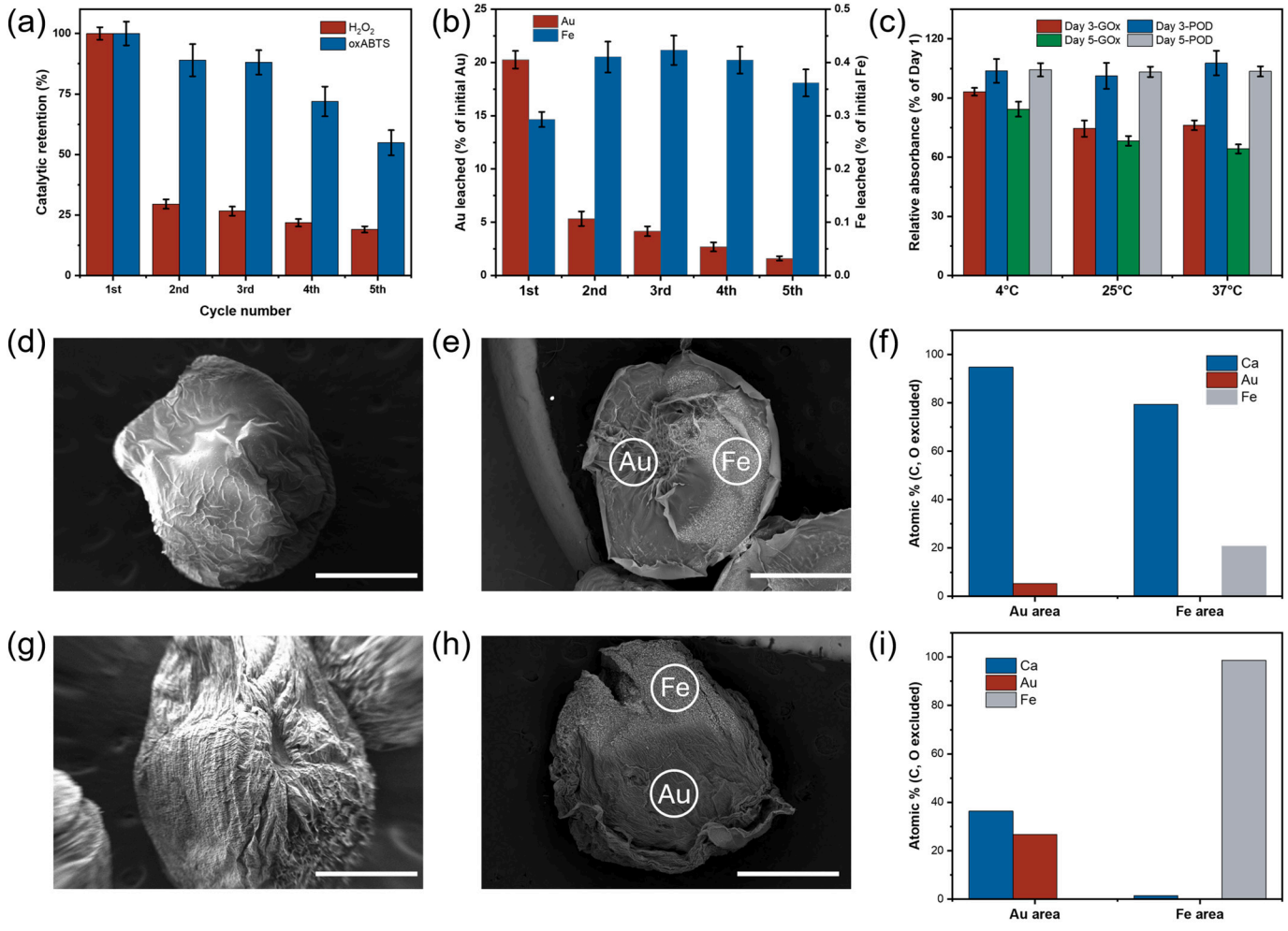

(j)

Group	Au	pH switch (9 → 2)	Fe_3O_4	Readout (% of ABTS)	Binary (O)
G1	0	0	0	0	0
G2	1	0	1	0	0
G3	0	1	1	0	0
G4	1	1	0	50	0
G5	1	1	1	100	1

(k)

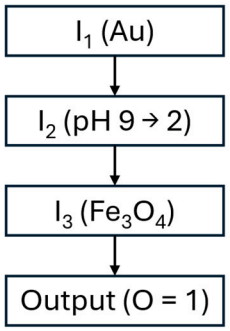

Fig. 6. (a) Retained activity of the GOx-like and POD-like steps over five cycles, normalized to the first use. (b) ICP-MS measured leaching of Au and Fe in each cycle (reported as % of the initial loading). (c) Storage stability at 4 °C, 25 °C and 37 °C on Day 3 and Day 5, each normalized to Day 1 at 25 °*C.* SEM/EDS characterization of the core-shell beads before and after use, (d,e) surface and cross-section SEM show a well-defined core-shell with separated Au and Fe domains, and (f) area-EDS confirms Ca/Au in the Au domain and Ca/Fe in the Fe domain before use; (g,h) surface and cross-section SEM indicate preserved core–shell morphology, and (i) area-EDS verifies that Au and Fe remain confined to their respective compartments after use. Scale bars is 500 μm. (j) Truth table for the pH-triggered order logic gate. (k) Logic-gate output diagram illustrating the sequence-dependent operation of the Au/pH/Fe_3O_4 system.

quantified the metal loss in the supernatant after each cycle using ICP-MS (Fig. 6b). Au loss was about 20 % in cycle 1 of the initial loading and then decreased only a few percent in cycles 2 to 5, consistent with the observed decrease in the GOx-like absorbance. By contrast, Fe loss per cycle was 0.4 % of the initial Fe loading, indicating a trace dissolution of Fe_3O_4 during the acidic step. Even there is substantial loss of Au in the cycle 1, the amount of H_2O_2 produced in subsequent cycles is sufficient for POD-like reaction to oxidize ABTS to high extent.

We next examined long-term storage at 4 °C, 25 °C and 37 °C. Beads were stored for 5 days, and activities were measured at Day 3 and Day 5 and normalized to the value on Day 1 (Fig. 6c). The GOx-like step was temperature-sensitive; activity on Day 5 remained at 85 % at 4 °C, 70 % at 25 °C and dropped to 60 % at 37 °C. By contrast, the POD-like step showed no loss at any temperature after 5 days. These results suggest that 4 °C storage is the preferred condition for better preserving the Au-driven first step.

To examine whether pH switching affects the architecture of the beads, we imaged the same core-shell beads before use and after the reactions. Surface and cross-section SEM (Fig. 6d-h) show an intact core-shell morphology without collapse. Area-EDS taken from the Au region and the Fe region, reported as inorganic-normalized atomic %, confirmed that Au and Fe are confined to their respective compartments before and after reactions. The decrease in Ca is observed, consistent with partial de-crosslinking during operation, but no loss of compartmentalization is detected.

Molecular logic gate converts chemical or environment inputs into binary outputs (1 or 0), following Boolean operations that enable clear decision-making in sensing and catalysis [67]. Unlike conventional spectroscopic detection that relies on gradual intensity changes, logic-gate design translates chemical responses into discrete "on/off" signals, making the system easier to interpret and less prone to false positives [68,69]. Inspired by these concepts, our compartmentalized hydrogel beads utilize distinct pH windows and spatially separated nanozymes to encode a three-input, sequence-dependent logic gate (Fig. 6j-k). Here, "1" is used to represent a true or high signal and "0" corresponds to a false or low signal [70]. I_1 corresponds to the presence of Au, I_2 to the completion of the pH transition from 9 to 2 and I_3 to the presence of the Fe_3O_4. Only when $[I_1, I_2, I_3] = [1]$ does the system generate H_2O_2 at pH 9 and subsequently oxidize ABTS at pH 2, yielding the digital output $O = 1$, while all other combinations give $O = 0$. This establishes a simple binary platform for ordered, compartmentalized catalysis, in which the output depends on both the correct components and their operation sequence, essential feature for reliable logic-gated sensing.

Building on this framework, we are currently advancing multi-compartment hydrogels where distinct domains house nanozymes targeting degradation of oppositely charged pollutants. Programmed pH switches will activate the appropriate compartment for selective capture and degradation, with the logic readout confirming correct sequence. These results will be reported separately.

4. Conclusion

In this study, we built a dual-compartment Alg bead that enables a sequential two-step nanozyme reaction under pH control, Au drives glucose oxidation at pH 9 to generate H_2O_2, and Fe_3O_4 performs ABTS oxidation at pH 2. Kinetic analysis showed that sequential reactions follow PSO behaviour, and the corresponding free nanozymes obey Michaelis–Menten kinetics. Mechanistically, Fe_3O_4 suppresses the Au-driven step in free solution and in single beads, but core-shell partitioning mitigates this interaction. Encapsulation in alginate also largely buffers the inhibition observed for the POD-like step in the free Au/Fe_3O_4 mixture, making the embedded Au/Fe_3O_4 comparable to Fe_3O_4 alone. Although both Au and Fe_3O_4 exhibit measurable leaching, the beads remain effective for at least four cycles, and activity is best preserved by storage at 4 °C. Finally, the sequential reactions can be encoded as an order-dependent logic gate that yields a robust digital output. Together, these results establish spatially separated nanozyme systems as a programmable way to ordered multistep catalysis with robust readouts.

CRediT authorship contribution statement

Hui Yang: Writing – original draft, Visualization, Methodology, Investigation, Formal analysis, Data curation, Conceptualization. **Catherine P. Whitby:** Writing – review & editing, Methodology, Conceptualization. **Jadranka Travas-Sejdic:** Writing – review & editing, Supervision, Project administration, Formal analysis, Data curation.

Declaration of competing interest

The authors declare that they have no known competing financial interests or personal relationships that could have appeared to influence the work reported in this paper.

Acknowledgements

This work was supported by the Reconfigurable Systems Research Program of the MacDiarmid Institute for Advanced Materials and Nanotechnology, New Zealand. We acknowledge the University of Auckland Shared Research Equipment Platform (ShaRE) and Dr. Timothy Christopher for collecting powder X-ray diffraction data.

Appendix A. Supplementary data

Supplementary data to this article can be found online at https://doi.org/10.1016/j.cej.2025.170646.

Data availability

Data will be made available on request.

References

[1] W. Martin, Evolutionary origins of metabolic compartmentalization in eukaryotes, Philos. Trans. R. Soc. B Biol. Sci. 365 (2010) 847–855, https://doi.org/10.1098/rstb.2009.0252.
[2] A. Honigmann, A. Pralle, Compartmentalization of the cell membrane, J. Mol. Biol. 428 (2016) 4739–4748, https://doi.org/10.1016/j.jmb.2016.09.022.
[3] M. Schrader, L.F. Godinho, J.L. Costello, M. Islinger, The different facets of organelle interplay - an overview of organelle interactions, front. Cell, Dev. Biol. 3 (2015) 1–22, https://doi.org/10.3389/fcell.2015.00056.
[4] C. Greening, T. Lithgow, Formation and function of bacterial organelles, Nat. Rev. Microbiol. 18 (2020) 677–689, https://doi.org/10.1038/s41579-020-0413-0.
[5] C. Guindani, L.C. da Silva, S. Cao, T. Ivanov, K. Landfester, Synthetic cells: from simple bio-inspired modules to sophisticated integrated systems, Angew. Chem. 134 (2022), https://doi.org/10.1002/ange.202110855.
[6] A.I. Benítez-Mateos, D. Roura Padrosa, F. Paradisi, Multistep enzyme cascades as a route towards green and sustainable pharmaceutical syntheses, Nat. Chem. 14 (2022) 489–499, https://doi.org/10.1038/s41557-022-00931-2.
[7] D. Tian, R. Hao, X. Zhang, H. Shi, Y. Wang, L. Liang, H. Liu, H. Yang, Multi-compartmental MOF microreactors derived from Pickering double emulsions for chemo-enzymatic cascade catalysis, Nat. Commun. 14 (2023) 1–14, https://doi.org/10.1038/s41467-023-38949-w.
[8] A. Belluati, S. Thamboo, A. Najer, V. Maffeis, C. von Planta, I. Craciun, C. G. Palivan, W. Meier, Multicompartment polymer vesicles with artificial organelles for signal-triggered cascade reactions including cytoskeleton formation, Adv. Funct. Mater. 30 (2020), https://doi.org/10.1002/adfm.202002949.
[9] H. Wang, Z. Zhao, Y. Liu, C. Shao, F. Bian, Y. Zhao, Biomimetic enzyme cascade reaction system in microfluidic electrospray microcapsules, Sci. Adv. 4 (2018), https://doi.org/10.1126/sciadv.aat2816.
[10] M.E. Allen, J.W. Hindley, D.K. Baxani, O. Ces, Y. Elani, Hydrogels as functional components in artificial cell systems, Nat. Rev. Chem. 6 (2022) 562–578, https://doi.org/10.1038/s41570-022-00404-7.
[11] H. Tan, S. Guo, N.D. Dinh, R. Luo, L. Jin, C.H. Chen, Heterogeneous multi-compartmental hydrogel particles as synthetic cells for incompatible tandem reactions, Nat. Commun. 8 (2017) 1–10, https://doi.org/10.1038/s41467-017-00757-4.
[12] Q. Qu, X. Zhang, A. Yang, J. Wang, W. Cheng, A. Zhou, Y. Deng, R. Xiong, C. Huang, Spatial confinement of multi-enzyme for cascade catalysis in cell-

inspired all-aqueous multicompartmental microcapsules, J. Colloid Interface Sci. 626 (2022) 768–774, https://doi.org/10.1016/j.jcis.2022.06.128.
[13] Y. Xi, B.D. Frank, A. Tatas, M. Pavlovic, L. Zeininger, Multicompartment calcium alginate microreactors to reduce substrate inhibition in enzyme cascade reactions, Soft Matter 19 (2023) 7541–7549, https://doi.org/10.1039/d3sm00816a.
[14] J. Li, D.J. Mooney, Designing hydrogels for controlled drug delivery, Nat. Rev. Mater. 1 (2016) 1–17, https://doi.org/10.1038/natrevmats.2016.71.
[15] H. Yang, C.P. Whitby, J. Travas-Sejdic, Dual-network hydrogel capsules for controlled molecular transport via pH and temperature responsiveness, J. Colloid Interface Sci. 677 (2025) 942–951, https://doi.org/10.1016/j.jcis.2024.08.119.
[16] A. Sharma, G. Gupta, T. Ahmad, S. Mansoor, B. Kaur, Enzyme engineering: current trends and future perspectives, Food Rev. Int. 37 (2021) 121–154, https://doi.org/10.1080/87559129.2019.1695835.
[17] M. Liang, X. Yan, Nanozymes: from new concepts, mechanisms, and standards to applications, Acc. Chem. Res. 52 (2019) 2190–2200, https://doi.org/10.1021/acs.accounts.9b00140.
[18] X. Geng, X. Du, W. Wang, C. Zhang, X. Liu, Y. Qu, M. Zhao, W. Li, M. Zhang, K. Tu, Y.Q. Li, Confined cascade metabolic reprogramming nanoreactor for targeted alcohol detoxification and alcoholic liver injury management, ACS Nano 17 (2023) 7443–7455, https://doi.org/10.1021/acsnano.2c12075.
[19] Z. Sun, H. Liu, M. Yin, N. Cheng, W. Liu, K. Zhao, H. Zeng, X. Chen, Z. Wang, X. Zhou, X. Zhao, F. Chen, Ruthenium nanozyme@magnesium silicate nanosheets encapsuled in microneedle patches promote repair of radiation-induced skin defects by remodeling pathological environment, Interdiscip. Med. 3 (2025), https://doi.org/10.1002/INMD.20240124.
[20] Q. Wang, H. Wei, Z. Zhang, E. Wang, S. Dong, Nanozyme: an emerging alternative to natural enzyme for biosensing and immunoassay, Trends Anal. Chem. 105 (2018) 218–224, https://doi.org/10.1016/j.trac.2018.05.012.
[21] M. Zhang, W. Tong, Stimuli-responsive nanozymes for biomedical applications, Biomater. Sci. 11 (2023) 5769–5780.
[22] B.N. Zope, D.D. Hibbitts, M. Neurock, R.J. Davis, Reactivity of the gold/water interface during selective oxidation catalysis, Science 80 (330) (2010) 74–78.
[23] L. Gao, J. Zhuang, L. Nie, J. Zhang, Y. Zhang, N. Gu, T. Wang, J. Feng, D. Yang, S. Perrett, X. Yan, Intrinsic peroxidase-like activity of ferromagnetic nanoparticles, Nat. Nanotechnol. 2 (2007) 577–583, https://doi.org/10.1038/nnano.2007.260.
[24] D. Ma, A. Liu, S. Li, C. Lu, C. Chen, TiO_2 photocatalysis for C-C bond formation, Catal, Sci. Technol. 8 (2018) 2030–2045, https://doi.org/10.1039/c7cy01458a.
[25] Y. Sun, Z. Li, J. Wu, Z. Wang, Y. Dong, H. Wang, J.L. Brash, L. Yuan, H. Chen, Gold nanoparticle-protein conjugate dually-responsive to pH and temperature for modulation of enzyme activity, J. Mater. Chem. B 7 (2019) 3260–3267, https://doi.org/10.1039/c9tb00325h.
[26] D. Sun, X. Pang, Y. Cheng, J. Ming, S. Xiang, C. Zhang, P. Lv, C. Chu, X. Chen, G. Liu, N. Zheng, Ultrasound-switchable nanozyme augments sonodynamic therapy against multidrug-resistant bacterial infection, ACS Nano 14 (2020) 2063–2076, https://doi.org/10.1021/acsnano.9b08667.
[27] M. Zhang, W. Tong, Stimuli-responsive nanozymes for biomedical applications, Biomater. Sci. 11 (2023) 5769–5780, https://doi.org/10.1039/d3bm00884c.
[28] R.J.R.W. Peters, M. Marguet, S. Marais, M.W. Fraaije, J.C.M. Van Hest, S. Lecommandoux, Cascade reactions in multicompartmentalized polymersomes, Angew, Chemie 126 (2014) 150–154, https://doi.org/10.1002/anie.201308141.
[29] Y. Cai, L. Zhang, W. Cheng, W. Xu, K. Yuan, R. Xiong, C. Huang, Compartmentalized encapsulated multienzyme chitosan-based three-compartment microspheres enable orderly multienzyme cascade reactions and blood sugar control, ACS Sustain. Chem. Eng. (2025), https://doi.org/10.1021/acssuschemeng.5c02095.
[30] S.C. Shetty, N. Yandrapalli, K. Pinkwart, D. Krafft, T. Vidakovic-Koch, I. Ivanov, T. Robinson, Directed signaling cascades in monodisperse artificial eukaryotic cells, ACS Nano 15 (2021) 15656–15666, https://doi.org/10.1021/acsnano.1c04219.
[31] A. Gole, C.J. Murphy, Seed-mediated synthesis of gold nanorods: role of the size and nature of the seed, Chem. Mater. 16 (2004) 3633–3640, https://doi.org/10.1021/cm0492336.
[32] A.H.F. Lee, S.F. Gessert, Y. Chen, N.V. Sergeev, B. Haghiri, Preparation of iron oxide silica particles for Zika viral RNA extraction, Heliyon 4 (2018) e00572, https://doi.org/10.1016/j.heliyon.2018.e00572.
[33] T.M. Gill, X. Zheng, Comparing methods for quantifying electrochemically accumulated H_2O_2, Chem. Mater. 32 (2020) 6285–6294, https://doi.org/10.1021/acs.chemmater.0c02010.
[34] L. Wang, B. Li, D.D. Dionysiou, B. Chen, J. Yang, J. Li, Overlooked formation of H_2O_2 during the hydroxyl radical-scavenging process when using alcohols as scavengers, Environ. Sci. Technol. 56 (2022) 3386–3396, https://doi.org/10.1021/acs.est.1c03796.
[35] D. Belhateche, J.M. Symons, Using cobalt-ultraviolet spectrophotometry to measure hydrogen peroxide concentration in organically laden groundwaters, Am. Water Work. Assoc. 83 (1991) 70–73, https://doi.org/10.1002/j.1551-8833.1991.tb07202.x.
[36] S. Chen, F. Huang, L. Mao, Z. Zhang, H. Lin, Q. Yan, X. Lu, J. Shi, High Fe-loading single-atom catalyst boosts ROS production by density effect for efficient antibacterial therapy, Nano-Micro Lett. 17 (2025) 1–17, https://doi.org/10.1007/s40820-024-01522-1.
[37] R.V. Lloyd, P.M. Hanna, R.P. Mason, The origin of the hydroxyl radical oxygenin the Fenton reaction, Free Radic. Biol. Med. 22 (1997) 885–888, https://doi.org/10.1016/S0891-5849(96)00432-7.
[38] R.G. Zepp, B.C. Faust, H. Jürg, Hydroxyl radical formation in aqueous reactions (pH 3-8) of Iron(II) with hydrogen peroxide: the photo-Fenton reaction, Environ. Sci. Technol. 26 (1992) 313–319, https://doi.org/10.1021/es00026a011.
[39] S.H. Bossmann, E. Oliveros, S. Göb, S. Siegwart, E.P. Dahlen, L. Payawan, M. Straub, M. Wörner, A.M. Braun, New evidence against hydroxyl radicals as reactive intermediates in the thermal and photochemically enhanced Fenton reactions, J. Phys. Chem. A 102 (1998) 5542–5550, https://doi.org/10.1021/jp980129j.
[40] D.D. Li, X. Gu, V. Timchenko, Q.N. Chan, A.C.Y. Yuen, G.H. Yeoh, Study of morphology and optical properties of gold nanoparticle aggregates under different pH conditions, Langmuir 34 (2018) 10340–10352, https://doi.org/10.1021/acs.langmuir.8b01457.
[41] Â. Barreto, L.G. Luis, A.V. Girão, T. Trindade, A.M.V.M. Soares, M. Oliveira, Behavior of colloidal gold nanoparticles in different ionic strength media, J. Nanopart. Res. 17 (2015) 1–13, https://doi.org/10.1007/s11051-015-3302-0.
[42] N.G. Khlebtsov, Determination of size and concentration of gold nanoparticles from extinction spectra, Anal. Chem. 80 (2008) 6620–6625, https://doi.org/10.1021/ac800834n.
[43] N.J. Lang, B. Liu, J. Liu, Characterization of glucose oxidation by gold nanoparticles using nanoceria, J. Colloid Interface Sci. 428 (2014) 78–83, https://doi.org/10.1016/j.jcis.2014.04.025.
[44] J. Chen, Q. Ma, M. Li, D. Chao, L. Huang, W. Wu, Y. Fang, S. Dong, Glucose-oxidase like catalytic mechanism of noble metal nanozymes, Nat. Commun. 12 (2021) 1–9, https://doi.org/10.1038/s41467-021-23737-1.
[45] M. Comotti, C. Della Pina, R. Matarrese, M. Rossi, The catalytic activity of "naked" gold particles, Angew. Chem. 116 (2004) 5936–5939, https://doi.org/10.1002/ange.200460446.
[46] M. Comotti, C. Della Pina, E. Falletta, M. Rossi, Aerobic oxidation of glucose with gold catalyst: hydrogen peroxide as intermediate and reagent, Adv. Synth. Catal. 348 (2006) 313–316, https://doi.org/10.1002/adsc.200505389.
[47] M.M. Montemore, M.A. Van Spronsen, R.J. Madix, C.M. Friend, O_2 activation by metal surfaces: implications for bonding and reactivity on heterogeneous catalysts, Chem. Rev. 118 (2018) 2816–2862, https://doi.org/10.1021/acs.chemrev.7b00217.
[48] S. Tian, C. Zhang, M. Yu, Y. Li, L. Fan, X. Li, Buffer species-dependent catalytic activity of cu-adenine as a laccase mimic for constructing sensor array to identify multiple phenols, Anal. Chim. Acta 1204 (2022) 339725, https://doi.org/10.1016/j.aca.2022.339725.
[49] F.J. Vernerey, S. Lalitha Sridhar, A. Muralidharan, S.J. Bryant, Mechanics of 3D cell-hydrogel interactions: experiments, models, and mechanisms, Chem. Rev. 121 (2021) 11085–11148, https://doi.org/10.1021/acs.chemrev.1c00046.
[50] S. Lagergren, About the Theory of So-Called Adsorption of Soluble Substances, 1898.
[51] G. Blanchard, M. Maunaye, G. Martin, Removal of heavy metals from waters by means of natural zeolites, Water Res. 18 (1984) 1501–1507, https://doi.org/10.1016/0043-1354(84)90124-6.
[52] E.D. Revellame, D.L. Fortela, W. Sharp, R. Hernandez, M.E. Zappi, Adsorption kinetic modeling using pseudo-first order and pseudo-second order rate laws: a review, Clean. Eng. Technol. 1 (2020) 100032, https://doi.org/10.1016/j.clet.2020.100032.
[53] S. Basak, S. Sikdar, S. Ali, M. Mondal, M.N. Roy, Green synthesized copper assisted iron oxide nanozyme for the efficient elimination of industrial pollutant via peroxodisulfate activation, J. Mol. Struct. 1283 (2023) 135267, https://doi.org/10.1016/j.molstruc.2023.135267.
[54] M.A. Komkova, A.A. Kostyukov, A.A. Shneiderman, V.A. Kuzmin, A.A. Karyakin, Fast reaction of the prussian blue based nanozyme "artificial peroxidase" with the substrates: pre-steady-state kinetic approach, J. Phys. Chem. Lett. 15 (2024) 8642–8649, https://doi.org/10.1021/acs.jpclett.4c01545.
[55] Y.S. Ho, G. McKay, Pseudo-second order model for sorption processes, Process Biochem. 34 (1999) 451–465, https://doi.org/10.1021/acs.oprd.7b00090.
[56] L. Xu, J. Chen, Q. Ma, D. Chao, X. Zhu, L. Liu, J. Wang, Y. Fang, S. Dong, Critical evaluation of the glucose oxidase-like activity of gold nanoparticles stabilized by different polymers, Nano Res 16 (2023) 4758–4766, https://doi.org/10.1007/s12274-022-5218-1.
[57] W. Luo, C. Zhu, S. Su, D. Li, Y. He, Q. Huang, C. Fan, Self-catalyzed, self-limiting growth of glucose oxidase-mimicking gold nanoparticles, ACS Nano 4 (2010) 7451–7458, https://doi.org/10.1021/nn102592h.
[58] H. Dong, W. Du, J. Dong, R. Che, F. Kong, W. Cheng, M. Ma, N. Gu, Y. Zhang, Depletable peroxidase-like activity of Fe_3O_4 nanozymes accompanied with separate migration of electrons and iron ions, Nat. Commun. 13 (2022), https://doi.org/10.1038/s41467-022-33098-y.
[59] G. Bae, M.W. Chung, S.G. Ji, F. Jaouen, C.H. Choi, pH effect on the H_2O_2-induced deactivation of Fe-N-C catalysts, ACS Catal. 10 (2020) 8485–8495, https://doi.org/10.1021/acscatal.0c00948.
[60] S.A. Walling, W. Um, C.L. Corkhill, N.C. Hyatt, Fenton and Fenton-like wet oxidation for degradation and destruction of organic radioactive wastes, Npj Mater. Degrad. 5 (2021) 1–20, https://doi.org/10.1038/s41529-021-00192-3.
[61] Z.M. Galbács, L.J. Csányi, Alkali-induced decomposition of hydrogen peroxide, J. Chem. Soc. Dalton Trans. (1983) 2353–2357, https://doi.org/10.1039/DT9830002353.
[62] E.G.P. Stender, S. Khan, R. Ipsen, F. Madsen, P. Hägglund, M.A. Hachem, K. Almdal, P. Westh, B. Svensson, Effect of alginate size, mannuronic/guluronic acid content and pH on particle size, thermodynamics and composition of complexes with β-lactoglobulin, Food Hydrocoll. 75 (2018) 157–163, https://doi.org/10.1016/j.foodhyd.2017.09.001.
[63] A. Cruz, L. Couto, S. Esplugas, C. Sans, Study of the contribution of homogeneous catalysis on heterogeneous Fe(III)/alginate mediated photo-Fenton process, Chem. Eng. J. 318 (2017) 272–280, https://doi.org/10.1016/j.cej.2016.09.014.

[64] P.C. Fung, K.M. Sin, S.M. Tsui, Decolorisation and degradation kinetics of reactive dye wastewater by a UV/ultrasonic/peroxide system, J. Soc. Dye. Colour. 116 (2000) 170–173, https://doi.org/10.1111/j.1478-4408.2000.tb00036.x.
[65] S.S. Kulkarni, C.A. Liao, C.T. Wu, S. Chattopadhyay, Enhanced reactive oxygen species mediated dye-degradation by H_2O_2 activation with different MoS2 nanostructures, J. Ind. Eng. Chem. (2025), https://doi.org/10.1016/j.jiec.2025.02.033.
[66] V.D. Doan, Q.H. Pham, B.A. Huynh, T.L.H. Nguyen, A.T. Nguyen, T.D. Nguyen, Kinetic analysis of nitrophenol reduction and colourimetric detection of hydrogen peroxide based on gold nanoparticles catalyst biosynthesised from Cynomorium songaricum, J. Environ. Chem. Eng. 9 (2021) 106590, https://doi.org/10.1016/j.jece.2021.106590.
[67] Y. Dong, S. Feng, W. Huang, X. Ma, Algorithm in chemistry: molecular logic gate-based data protection, Chem. Soc. Rev. 54 (2025) 3681–3735, https://doi.org/10.1039/d4cs01104j.
[68] C.P.M. de Silva, A. Prasanna, Nimal H.Q. Gunaratne, A molecular photoionic AND gate based on fluorescent signlling, Nature 364 (1993) 42–44.
[69] L. Liu, P. Liu, L. Ga, J. Ai, Advances in applications of molecular logic gates, ACS Omega 6 (2021) 30189–30204, https://doi.org/10.1021/acsomega.1c02912.
[70] S. Erbas-Cakmak, S. Kolemen, A.C. Sedgwick, T. Gunnlaugsson, T.D. James, J. Yoon, E.U. Akkaya, Molecular logic gates: the past, present and future, Chem. Soc. Rev. 47 (2018) 2228–2248, https://doi.org/10.1039/c7cs00491e.